Spontaneous time-reversal symmetry breaking from interference-selected Josephson-island winding states

Henry Sheehy[1, 2]

[1] *School of Physical Sciences, University of Kent, Canterbury CT2 7NH, United Kingdom*
[2] *QuantaLumin*

(Dated: July 2, 2026)

We study spontaneous loop-supercurrent selection in reduced superconducting circuits with attractive superconducting regions coupled through repulsive normal channels. The mechanism is interference selection: a phase texture can lower the energy when destructive interference suppresses anomalous density on a costly normal region. Compact C3 molecules provide the clean analytic rule, because the $m = \pm 1$ winding textures satisfy $1 + \omega + \omega^2 = 0$ and therefore node an active central repulsive site. Compact C4 molecules and clusters expose the main square-geometry difficulty: staggered order also nodes the centre and naturally cancels nearest-neighbour normal paths, so a square loop requires separated diagonal or outer channels to make winding uniquely favourable. Naive compact onsite-Hubbard molecules, clusters, tubes, and screw-cell crystals preserve the winding texture but remain too stiff or too amplitude-starved to make it the robust ground state. A tuned C3 signed crystal-bath molecule gives a positive small-model HFG existence smoke: the central positive-U site is updated self-consistently, the uniform branch develops a central antinode, and the winding branches retain the symmetry node. A C4 split-centre crystal-bath prototype likewise supports finite-amplitude winding rows once pair-susceptible reservoir orbitals are added to the square selector geometry. We then separate condensate formation from phase selection in a Josephson-island model. For a long, soft outer-channel device we find a strict self-consistent Hartree–Fock–Gor'kov winding minimum with degenerate time-reversed partners, $F_{\mathrm{wind}} - F_{\mathrm{nonwind}} \simeq -2.386 \times 10^{-3}$, and a maximum residual 4.996×10^{-5} for the stated 5×10^{-5} threshold. The result is finite-device HFG evidence that a time-reversal-symmetric Hamiltonian can select a time-reversal-breaking loop-current state without imposed flux or Peierls phases.

I. INTRODUCTION

Josephson circuits are a natural setting for phase frustration, weak-link current-phase relations, and current-carrying superconducting states [1–5]. The question addressed here is sharper than whether a current can be imposed by external flux. We ask whether a time-reversal-symmetric superconducting device can choose a pair of degenerate, time-reversed winding states as its self-consistent ground state. Known examples and analogues of time-reversal-symmetry-breaking (TRSB) pairing physics include the chiral phases of superfluid ^{3}He, unconventional superconducting order-parameter phenomenology, phase-sensitive cuprate tests, and nonunitary or multicomponent proposals for $LaNiC_2$ and $LaNiGa_2$ [6–11]. These settings are usually discussed in terms of unconventional order parameters, internal orbital or spin structure, or explicitly chiral pairing channels. The mechanism studied here is different. The pairing field is an otherwise conventional mean-field superconducting field on a real-space graph. Spontaneous TRSB is selected by interference and device geometry, not by inserting a chiral order parameter, an external flux, or Peierls phases. It is also distinct from spontaneous-current loops built from imposed or effective π-junction frustration, where the junction itself supplies a phase-shifted Josephson relation [12].

The central difficulty is that winding costs phase stiffness. A loop phase texture must twist around the device, and in a compact microscopic molecule that cost is large. The compensating energy scale is the repulsive-channel anomalous-density cost. On a site or channel with positive interaction, induced anomalous density κ raises the Gor'kov part of the mean-field energy; a phase texture can therefore gain energy if destructive interference places a node or strong suppression of κ on that region. We refer to this contribution below as the repulsive Gor'kov or anomalous-density penalty. The design problem is consequently concrete: the normal channel must carry anomalous-density antinodes in nonwinding branches, the winding branch must remove them by interference, and the channel must be long or soft enough that the saved repulsive energy exceeds the phase-stiffness cost.

Figure 1 gives the design rule in schematic form. Figure 2 then states the model ladder used in the rest of the paper, and Table I summarizes the mechanism tested and status of each rung. The sequence runs from C3 and C4 molecules, through signed C3/C4 crystal-bath checks, C3/C4 clusters, and a screw-separated C4 molecule, to tube, lattice, C4 screw-cell, proximity-film, and Josephson-island realizations. Compact C3 gives a clean node rule, while compact C4 exposes a staggered nonwinding competitor. Clusters, tubes, lattices, and films are intermediate diagnostics of amplitude support, stiffness, and geometry. The newer signed crystal-bath simulations show that pair-susceptible reservoir orbitals can compensate the Hartree amplitude loss in small microscopic models, while long, soft Josephson-island channels provide the strongest finite-device realization whose

static four-branch HFG free-energy comparison is the ground-state evidence. Supplemental Material and the accompanying verification bundle give the model-specific graph conventions, solver normalization, genetic-search parameters, final numerical-output tables, intermediate checks, and numerical figure data needed for independent verification. The computations in this work were performed using a private general-purpose codebase developed by the author. The code is not released because it implements a broader framework beyond the scope of this paper. To support independent verification, the paper, Supplemental Material, and verification bundle provide the mathematical specification of the cases studied, parameter choices, benchmark values, and numerical data underlying quantitative figures.

II. HAMILTONIAN AND SELF-CONSISTENCY

We consider finite tight-binding superconducting devices with attractive superconducting regions A and repulsive or normal regions N. All models in this paper are special cases of the real tight-binding Hamiltonian

$$H = \sum_{ij,\sigma} (h_{ij}^{(0)} - \mu\delta_{ij}) c_{i\sigma}^\dagger c_{j\sigma} + \sum_i U_i n_{i\uparrow} n_{i\downarrow}, \tag{1}$$

with $U_i < 0$ on superconducting islands and $U_i > 0$ or no attractive instability on normal sites. For the island calculations below the same local interaction profile is written in region language: $U_i = -U$ on superconducting islands, $U_i = +V$ on inner normal channels, and $U_i = +W$ on outer normal channels. All hoppings and interaction constants are real, so Eq. (1) is time-reversal symmetric; no flux or Peierls phase is imposed.

The HFG/BdG reduction proceeds in a fixed order. The normal and anomalous contractions are

$$\rho_{i\sigma,j\sigma'} = \langle c_{j\sigma'}^\dagger c_{i\sigma} \rangle, \qquad \kappa_i = \langle c_{i\downarrow} c_{i\uparrow} \rangle. \tag{2}$$

For the onsite interaction, Wick factorization gives

$$\begin{aligned} n_{i\uparrow} n_{i\downarrow} \simeq\ & \langle n_{i\uparrow} \rangle n_{i\downarrow} + n_{i\uparrow} \langle n_{i\downarrow} \rangle - \langle n_{i\uparrow} \rangle \langle n_{i\downarrow} \rangle \\ & + \kappa_i c_{i\uparrow}^\dagger c_{i\downarrow}^\dagger + \kappa_i^* c_{i\downarrow} c_{i\uparrow} - |\kappa_i|^2. \end{aligned} \tag{3}$$

The spin-flip Fock terms vanish in the nonmagnetic island ansatz used for the accepted results, but they remain part of the general HFG bookkeeping for unrestricted microscopic checks. The resulting quadratic HFG Hamiltonian is

$$\begin{aligned} H_{\mathrm{HFG}} =\ & \sum_{ij,\sigma} (h_{ij}^{(0)} + \Sigma_{ij,\sigma}) c_{i\sigma}^\dagger c_{j\sigma} \\ & + \sum_i \left(\Delta_i c_{i\uparrow}^\dagger c_{i\downarrow}^\dagger + \Delta_i^* c_{i\downarrow} c_{i\uparrow} \right) + E_{\mathrm{dc}}, \end{aligned} \tag{4}$$

with local fields

$$\Sigma_{ii,\uparrow} = U_i \langle n_{i\downarrow} \rangle, \qquad \Sigma_{ii,\downarrow} = U_i \langle n_{i\uparrow} \rangle, \qquad \Delta_i = U_i \kappa_i. \tag{5}$$

The double-counting constant subtracts the inserted contractions,

$$E_{\mathrm{dc}} = -\sum_i U_i \left(\langle n_{i\uparrow} \rangle \langle n_{i\downarrow} \rangle - |\kappa_i|^2 \right), \tag{6}$$

and is included in every branch free energy. The signs in Eq. (6) follow the signed onsite convention used here, $\Delta_i = U_i \kappa_i$; the finite-HFG implementation uses the same convention in the equivalent form $|\Delta_i|^2/(-U_i)$ for the pairing double-counting term. In the folded spin-singlet Nambu basis

$$\Psi = (c_{1\uparrow}, \ldots, c_{N\uparrow}, c_{1\downarrow}^\dagger, \ldots, c_{N\downarrow}^\dagger)^T, \tag{7}$$

the BdG matrix is

$$\mathcal{H}_{\mathrm{BdG}} = \begin{pmatrix} h^{(0)} + \Sigma_\uparrow - \mu & \Delta \\ \Delta^\dagger & -(h^{(0)} + \Sigma_\downarrow - \mu)^T \end{pmatrix}. \tag{8}$$

Self-consistency means recomputing ρ and κ from the occupied quasiparticle states of Eq. (8), updating Eq. (5), and iterating until the maximum field residual falls below the quoted tolerance. For a generic active field $\Phi_\alpha \in \{\Delta_i, \Sigma_i, \ldots\}$ the damped update is

$$\Phi_\alpha^{(m+1)} = (1-\gamma)\Phi_\alpha^{(m)} + \gamma \Phi_{\alpha,\mathrm{cand}}^{(m)}, \tag{9}$$

with residual

$$R^{(m)} = \max_{\alpha \in \mathcal{S}} \left| \Phi_{\alpha,\mathrm{cand}}^{(m)} - \Phi_\alpha^{(m)} \right|. \tag{10}$$

Linear mixing is used in difficult cases; the unresolved side points discussed below contract slowly rather than oscillating between two branch solutions.

The branch free energy is evaluated from the BdG spectrum and double-counting terms. At $T = 0$ the implementation records the common folded-spin convention

$$\begin{aligned} F_{\mathrm{HFG}} =\ & -\frac{1}{2} \sum_\nu |E_\nu| + \frac{1}{2} \operatorname{Tr} H_{ee} \\ & + F_{\mathrm{Gorkov}} + F_{\mathrm{Hartree}} + F_{\mathrm{Fock}}, \end{aligned} \tag{11}$$

where $H_{ee} = h^{(0)} + \Sigma_\uparrow - \mu$. The Gor'kov, Hartree, and Fock terms are the corresponding double-counting constants, decomposed by island, inner-channel, and outer-channel masks. The trace and folded-spin normalization are common to all branches, so branch ordering is unaffected by the convention. The decomposition is used to distinguish a genuine repulsive-channel saving from a trivial loss of superconducting amplitude [13]. The branch comparison criterion is then defined using

$$\mathcal{B} = \{u, s, +, -\}, \qquad \mathcal{B}_{\mathrm{non}} = \{u, s\}, \tag{12}$$

where u is uniform, s is staggered, and $\pm$ are the two winding branches. For every branch $b \in \mathcal{B}$ we report

$$F_{\mathrm{min}} = \min_{b \in \mathcal{B}} F_b, \qquad \Delta F_b = F_b - F_{\mathrm{min}}. \tag{13}$$

A branch is promoted only when all compared branches satisfy the same residual threshold. The two winding branches must also remain degenerate within the numerical tolerance expected for time-reversal partners.

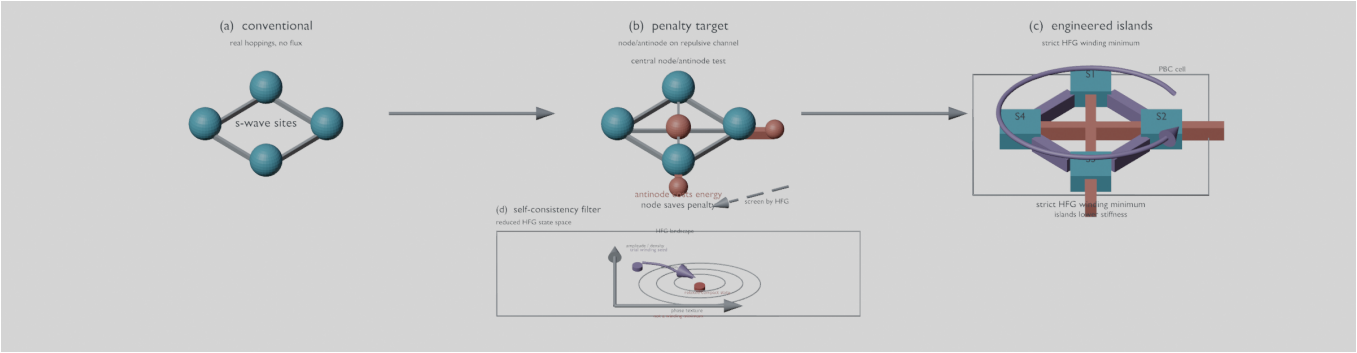

FIG. 1. Design-rule schematic for interference-selected spontaneous TRSB in a conventional superconducting mean-field device. The top row shows the physical design sequence: (a) A real-hopping, zero-flux cluster has no imposed circulation. (b) Repulsive normal regions define a node/antinode penalty that can distinguish branch textures. (c) Long, soft Josephson-island channels implement the same interference rule while lowering stiffness, giving the residual-controlled winding minimum tested below. The lower inset is a separate self-consistency filter: a winding-like seed must remain an HFG free-energy minimum in reduced state space, whereas isolated compact onsite-Hubbard models relax to amplitude-starved or nonwinding basins unless an amplitude reservoir is supplied. Blue and red spheres denote compact microscopic superconducting and repulsive orbitals; square blue pads and rectangular red channels denote the simplified engineered-island limit. Purple channels in (c) mark winding-favouring paths, and the grey frame marks the schematic PBC cell.

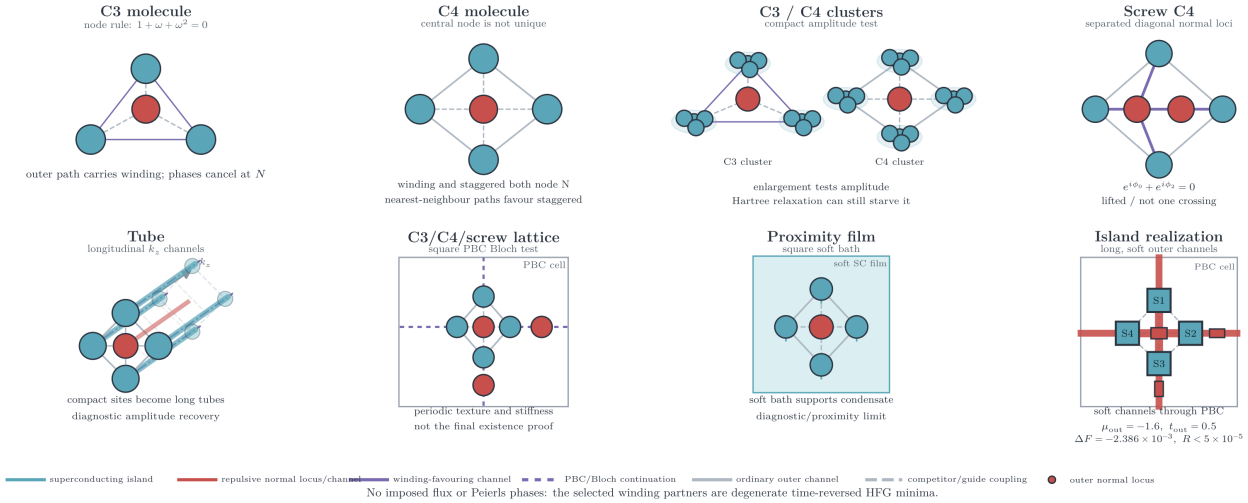

FIG. 2. Mechanism-to-device overview. Blue elements are superconducting sites, islands, clusters, tubes, or film support; red elements are repulsive normal loci or channels. Purple solid paths mark winding-favouring selector channels in schematic panels, solid grey paths mark ordinary outer channels, dotted segments mark PBC/Bloch continuations, and thin dashed grey paths mark competitor, guide, or diagnostic couplings. Active anomalous-density antinodes first have to appear on costly normal regions in nonwinding branches. The C3 molecule gives the phase-sum node $1+\omega+\omega^2=0$ on the central repulsive site. The C4 molecule shows why this is not enough: central-site cancellation is not unique to winding because staggered order also nodes the centre and can cancel nearest-neighbour normal paths. C3 and C4 clusters replace single attractive orbitals by compact attractive clusters and test whether microscopic enlargement restores amplitude, but Hartree relaxation can still suppress the anomalous density. The screw C4 molecule is a different geometry, not a cluster: it effectively splits the central normal node into separated diagonal loci, giving the winding branch a suppression pattern on those channels that the staggered branch does not share. Tube models promote compact sites into longitudinal one-dimensional channels, sketched as tubes extending along k_z, and test whether k_z averaging can restore superconducting amplitude; in the sampled microscopic rows they do not constitute the winding ground-state result. The C3/C4/screw-C4 lattice panel tests periodic stiffness and Bloch-structure effects; the right and bottom outer normal loci mark additional PBC-channel antinode/node tests. Proximity-film models instead test the supplied-amplitude limit through a soft superconducting environment, here drawn as a square film surrounding the active sites, and can show winding-favoured diagnostic windows, but they are not the strict ground-state evidence. The final island device extends compact sites into superconducting islands with red inner and outer normal channels; the PBC cell indicates how the outer channels wrap through the periodic construction. The islands support amplitude, while the soft outer channels reduce winding stiffness and retain a repulsive-channel saving.

A. Model specializations

The named intermediate models differ only in the one-body graph and in whether superconducting amplitude is self-generated or supplied. Compact clusters replace

TABLE I. Model ladder, mechanism tests, and status. The table separates constructive mechanism diagnostics from the final static HFG ground-state evidence. Listed variations are representative axes in the private-code scans rather than a raw inventory of every generated row. "Positive selector" means that the model realizes the intended winding-favouring interference rule in the diagnostic sense stated in the text, not that it by itself proves a broad stable phase.

Model	Mechanism tested	Result/status	Role in argument
C3 molecule	Four-site central-node, seven-site edge-extended, and signed crystal-bath molecules; central phase-sum cancellation, $1 + \omega + \omega^2 = 0$, on the repulsive site.	Clean analytic winding node. Tiny isolated onsite-Hubbard molecules remain amplitude-starved, but a tuned central-only signed crystal-bath HFG check selects the degenerate winding pair with finite active and bath amplitude.	Minimal interference rule and positive small-model smoke.
C4 molecule	Central-only, split-centre, baseline, and outside-junction compact variants test whether a square central node uniquely selects winding.	Central-only is negative as a selector: staggered order also nodes the centre and cancels nearest-neighbour normal paths; split/outside variants motivate the screw repair.	Identifies the C4 competitor.
C4 signed crystal bath	Split-centre and opposite-pair positive-U selectors coupled to pair-susceptible finite or dispersive reservoir orbitals; screened Hartree and projected or fully complex Fock controls.	Positive tuned reservoir prototype: finite-amplitude winding rows survive signed onsite HFG updates, screened Hartree feedback, and sampled fully complex Fock closure, but the result is not yet a thermodynamic or materials-realistic phase diagram.	Microscopic reservoir-band existence check.
C3 clusters	Compact attractive islands with $N_A =$ 1–3 sites, extended to $N_A = 6$; central-normal-cluster, density-control, continuation, and root-solve checks.	Ungated strict onsite-Hubbard roots remain Hartree-detuned and amplitude-starved; the largest mean attractive-island gap in the size-scaling scan is only 1.7×10^{-5}.	Shows finite cluster growth is insufficient.
C4 clusters	Baseline, central-only, screw-only, split-centre, balanced-shared, and balanced-screw variants with $N_A =$ 1–3, central-channel, outside-channel, t_{out}, and U_{out} scans.	Recovery scans remain amplitude-starved or nonwinding-led; constrained balanced-screw scans select winding on much of the grid, but unrestricted $N_A = 1, 2$ checks relax to essentially normal amplitudes.	Separates C4 phase selection from amplitude support.
Hartree-biased compact HFG	Density-relaxed onsite-Hubbard HFG with an added static Hartree-compensation field or island gate, so that the densities still relax but the attractive orbitals are biased back toward the target pairing window.	C3 molecule, C3 cluster, C4 split-centre, and balanced-screw C4 scans confirm that Hartree detuning is the failure mode for isolated compact onsite-Hubbard routes; hybrid cluster/channel refinements can give strict winding-led rows only with $\lvert\Delta_A\rvert \sim 10^{-5}$–$10^{-4}$.	Negative isolated-compact rescue; motivates reservoir baths, proximity support, or Josephson islands.
Screw C4 molecule	Split-centre and balanced-screw compact selector logic with separated diagonal normal loci, rather than a single planar crossing site.	Positive selector in constrained compact diagnostics; winding gets a channel-suppression pattern not shared by staggered order.	Repairs the C4 node rule.
Tube models	Promote C3 and balanced-screw C4 compact sites into longitudinal channels and average microscopic HFB fields over k_z.	Finite amplitude and node/antinode contrast can be recovered after tuning, but sampled rows do not provide a superconducting winding ground-state result; a softer-channel continuation crosses only after the winding amplitude collapses to $\sim 10^{-6}$.	Tests a banded microscopic rescue.
C3/C4 lattices	C3 intercell patterns and C4 central-only, split-centre, balanced-shared, and balanced-screw Bloch embeddings test whether an extended normal-electron background can supply the density/Hartree environment missing from compact molecules.	Diagnostic lattice screens clarify periodic-channel stiffness and Hartree-density feedback; full microscopic recovery remains normal or nonwinding-led in the sampled rows.	Tests extended density support, not only enlarged cells.
C4 screw-cell crystal	Finite-k screw-cell, contact/outer-geometry, constrained-release, and sign-frustrated microscopic searches.	Strongest microscopic near miss: a clean winding basin survives release, but the best rows remain slightly uniform-led, with margins of order 5–7×10^{-7}.	Near-degenerate bulk calibration, not a proof.
Proximity film	Supplied-amplitude limit: C3, C4 baseline, split, balanced-shared, and balanced-screw reduced, finite-patch, and k-space film diagnostics with a fixed proximity background in addition to any relaxed film response.	Restores nonzero anomalous amplitude for molecule tests and can show winding-favoured diagnostic windows, including a narrow balanced-screw finite-film point with $\lvert\Delta_{\mathrm{film}}\rvert \simeq 0.19$ and $\Omega_{\mathrm{wind}} - \Omega_{\mathrm{nonwind}} \simeq -4.1 \times 10^{-7}$ at residual $< 5 \times 10^{-7}$; a simple k-space	Demonstrates amplitude support.

each attractive orbital A_j by a set of attractive sites S_j:

$$\begin{aligned} H_{\rm cl} = & \sum_{j,a\in S_j,\sigma} (\epsilon_a - \mu) n_{a\sigma} - \sum_{(ab)\in E_S,\sigma} t_{ab} \left(c^\dagger_{a\sigma} c_{b\sigma} + \text{h.c.} \right) \\ & + H_{\rm normal}[C,B,N] - \sum_{(ar)\in E_{SN},\sigma} t_{ar} \left(c^\dagger_{a\sigma} c_{r\sigma} + \text{h.c.} \right) \\ & + \sum_{j,a\in S_j} U_A n_{a\uparrow} n_{a\downarrow} \\ & + \sum_{r\in N} U_r n_{r\uparrow} n_{r\downarrow}. \end{aligned} \tag{14}$$

Here E_S contains intra-cluster hopping, E_{SN} the contacts to the same normal loci used in the parent molecule, $U_A < 0$, and $U_r \geq 0$. C3 and C4 cluster scans therefore test finite attractive islands without changing the interference channels.

The Hartree-biased compact scans keep Eq. (14) density-relaxed but add a static compensating normal field,

$$H_{\rm Hbias} = H_{\rm cl} + \sum_{i,\sigma} \Sigma^{H,\rm ext}_{i\sigma} n_{i\sigma}, \qquad \Sigma^{H,\rm ext}_{i\sigma} = -\alpha U_i n^0_{i\bar\sigma}. \tag{15}$$

The self-consistent Hartree term $U_i n_{i\bar\sigma}$ is still solved; the parameter α only biases the relaxed level toward the chosen reference density.

Tube models promote each transverse molecule or cluster site into a one-dimensional periodic channel. For transverse Hamiltonian $h^\perp$ the normal block is

$$h_{ij}(k_z) = h^\perp_{ij} - 2t^z_i \cos k_z \, \delta_{ij}, \tag{16}$$

and

$$H_{\rm tube} = \sum_{k_z,ij,\sigma} \left[h_{ij}(k_z) - \mu\delta_{ij} \right] c^\dagger_{k_z i\sigma} c_{k_z j\sigma} + \sum_i U_i n_{i\uparrow} n_{i\downarrow}. \tag{17}$$

The HFG densities and anomalous fields are Brillouin-zone averages over k_z.

Bloch-lattice diagnostics instead repeat a finite motif in the plane. For orbital labels a, b inside a unit cell,

$$H_{\rm lat} = \sum_{\boldsymbol{k},ab,\sigma} \left[h_{ab}(\boldsymbol{k}) - \mu\delta_{ab} \right] c^\dagger_{\boldsymbol{k}a\sigma} c_{\boldsymbol{k}b\sigma} + \sum_a U_a n_{a\uparrow} n_{a\downarrow}, \tag{18}$$

with

$$h_{ab}(\boldsymbol{k}) = \epsilon_a \delta_{ab} - \sum_{\boldsymbol{R}} t_{ab}(\boldsymbol{R}) e^{\mathrm{i}\boldsymbol{k}\cdot\boldsymbol{R}}. \tag{19}$$

These calculations test whether a periodic normal-electron background supplies the density and Hartree environment that compact molecules lack.

The proximity-film calculations use the same active molecule Hamiltonian but add supplied condensate support. In the reduced form this is a branch-labelled anomalous self-energy,

$$H^{\rm red}_{\rm prox} = H_{\rm active} + \sum_{i\in A} \left(\eta_i e^{\mathrm{i}\phi_i} c^\dagger_{i\uparrow} c^\dagger_{i\downarrow} + \text{h.c.} \right), \tag{20}$$

where the phases ϕ_i label the tested branch. In the finite-film form the support is represented explicitly by film sites f:

$$\begin{aligned} H_{\rm film} &= H_{\rm active} + H_f - \sum_{if,\sigma} t_{if} \left(c^\dagger_{i\sigma} c_{f\sigma} + \text{h.c.} \right), \\ H_f &= \sum_{f,\sigma} \epsilon_f n_{f\sigma} + \sum_f U_f n_{f\uparrow} n_{f\downarrow}. \end{aligned} \tag{21}$$

These film models are supplied-amplitude diagnostics; they are not self-generated ground-state evidence.

III. INTERFERENCE SELECTION

For a repulsive normal site coupled symmetrically to islands with phases ϕ_j, the induced anomalous amplitude is controlled by a phase sum,

$$\kappa_N \propto \sum_j a_j e^{\mathrm{i}\phi_j}, \tag{22}$$

where a_j includes hopping and spectral weights. If symmetry or geometry makes this sum vanish, the positive-interaction region avoids a repulsive Gor'kov/anomalous-density cost.

This is not enough by itself. The free energy also contains the spectral cost of twisting the superconducting phase, Hartree/Fock relaxation, and competition with nonwinding phase patterns. The branch-selection criterion used throughout this work is therefore direct: all candidate branches are iterated under the same self-consistency standard, and the winner is the converged branch with the lowest HFG free energy. Current and time-dependent diagnostics are used only after the static branch is selected.

A. Geometry search procedure

Candidate geometries were generated in two stages. The first stage is a genetic search over cheap susceptibility and ADOS-like diagnostics, used only to propose promising island/channel layouts. Each genome specifies the parameters that move anomalous-density antinodes through the device: island and channel chemical potentials, attractive and repulsive interaction strengths, island separation, parity constraints on the separation, outer-strip width, outer-contact geometry, inner-sheet radius, corner rounding, and C4-compatible boundary choices. The initial population is drawn from the allowed search space, optionally supplemented by previously saved CSV candidates. Each genome is keyed by the quantized parameter tuple, with continuous controls rounded to three significant figures for duplicate detection. Each generation evaluates the susceptibility score for all unevaluated genomes in parallel, checkpoints the raw metrics to CSV, keeps an elite subset, breeds children by choosing each coordinate from one of two elite

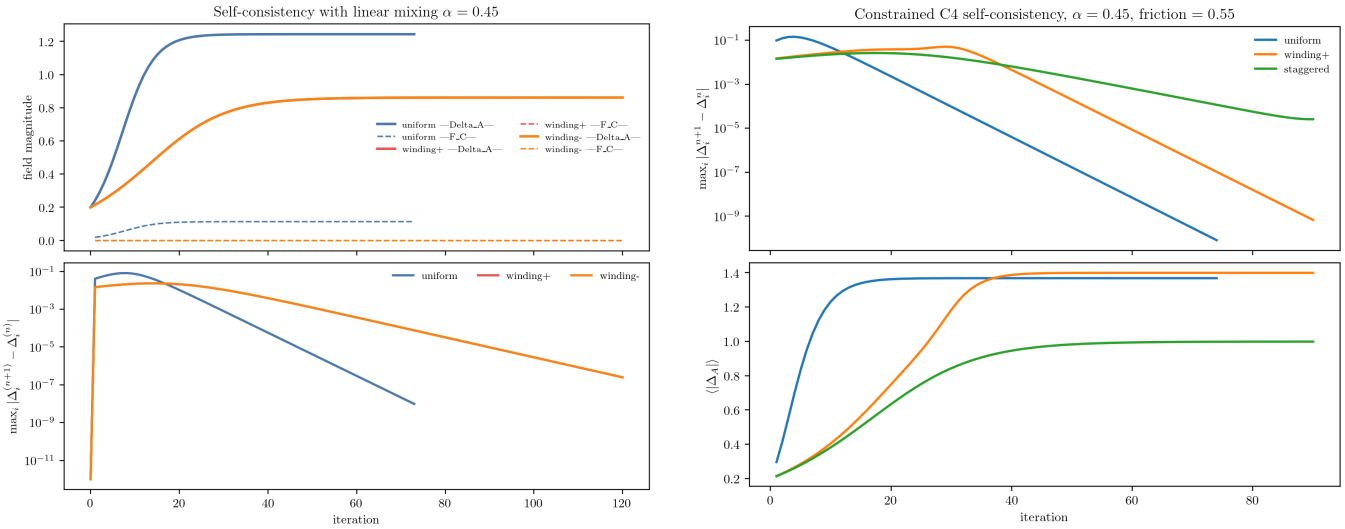

FIG. 3. Representative self-consistent mean-field iteration histories in the compact microscopic problems. Left: the C3 molecule with linear mixing $\alpha = 0.45$ shows the field amplitudes saturating and the maximum update residual decaying over iterations for uniform and winding seeds. Right: the constrained C4 molecule with $\alpha = 0.45$ and friction 0.55 shows uniform, winding, and staggered branches converging at different rates. These examples document that branch labels are followed by actual fixed-point iteration rather than by a one-shot imposed texture; the branch free energy after convergence remains the selection criterion.

parents with equal probability, mutates individual coordinates within the allowed profile, and injects random genomes to maintain exploration. Discrete mutations move by a normally distributed number of grid steps clipped to the allowed range; continuous mutations add a Gaussian displacement measured in the median grid step and are then clipped and requantized. The implemented susceptibility-screening stage defaults to a focused profile with a population of 96 points, 24 elites, 16 random injections, mutation probability 0.55, mutation width of two grid steps, eight generations, seed 20260514, and 24 worker processes. The active HFG-promotion stage uses smaller batches by default: 72 genomes, 18 elites, 12 random injections, six HFG promotions per generation, and local refinements around confirmed HFG elites.

The fitness is mechanism-facing rather than variational. It rewards a large anomalous response on outer or opposite-island repulsive loci that a winding phase can suppress, an outer-over-inner response advantage, and survival of anomalous density on the superconducting islands. It penalizes staggered outer saving, staggered inner saving, excessive raw response without selectivity, singular susceptibility outliers, and inner-node mechanisms that would naturally promote the staggered branch instead of winding. Thus the search is designed to find geometries where the winding node removes a real repulsive Gor'kov cost without simultaneously giving the same saving to a nonwinding competitor.

The second stage promotes only selected candidates to the expensive calculation. The active-search code sorts the accumulated susceptibility rows by this score, skips points whose complete branch/seed-family HFG coverage has already been evaluated, and promotes the highest-ranked distinct geometries. For each promoted geometry and parameter set, the HFG equations are run from uniform, staggered, winding +, and winding − seeds with common solver settings, and the branch free energies, residuals, and regional Hartree/Fock/Gor'kov decomposition are recorded. The active-search summary groups branch rows by geometry and parameters, requires the uniform and staggered families and at least one winding family to be present, and keeps the branch-wise lowest free energies across seed families for ranking and local refinement. This automated summary is still a candidate-promotion layer. The manuscript point is accepted only after a separate curated audit verifies the residual threshold, compares the four branch families, and checks that the two winding partners are degenerate within numerical tolerance. Only this strict four-branch free-energy comparison is used below as evidence for a ground-state winding result; the genetic search supplies candidates and diagnostics, not the selection evidence.

Implementation details of the search profiles, fitness terms, and active-search promotion settings are collected in Appendix A and tabulated in the verification bundle.

B. Ginzburg–Landau-scale interpretation

The microscopic free-energy decomposition has a simple coarse-grained reading. Writing island phases as ϕ_a and treating the island amplitudes as slowly varying gives a phase-only contribution of the form

$$F_{\mathrm{stiff}} \sim \sum_{\langle ab \rangle} J_{ab} \left[1 - \cos(\phi_a - \phi_b)\right], \tag{23}$$

which is the stiffness cost paid by a winding texture. The repulsive-channel part is instead controlled by induced anomalous density on normal regions,

$$F_{\rm rep} \sim \sum_{r\in N} U_r |\kappa_r(\{\phi_a\})|^2, \qquad U_r > 0. \tag{24}$$

Nonwinding branches can place antinodes of κ_r on the costly region, whereas a winding branch can reduce this term through destructive interference. The microscopic HFG calculation keeps the spectral, Hartree, Fock, and double-counting terms that this GL-scale expression suppresses. Thus the GL language is used only to identify stiffness cost versus repulsive-channel saving; it is not a broad phase-diagram derivation.

IV. MINIMAL C3 SELECTOR

The C3 molecule contains three attractive sites A_0, A_1, A_2 coupled to a central repulsive site C. The corresponding specialization of Eq. (1) is

$$\begin{aligned} H_{\rm C3} = &\sum_{j,\sigma} \epsilon_A n_{A_j\sigma} + \sum_{\sigma} \epsilon_C n_{C\sigma} \\ &- t_C \left(\mathcal{T}_C + \mathcal{T}_C^\dagger\right) - t_\ell \left(\mathcal{T}_\ell + \mathcal{T}_\ell^\dagger\right) \\ &+ \sum_j U_A n_{A_j\uparrow} n_{A_j\downarrow} + U_C n_{C\uparrow} n_{C\downarrow}, \end{aligned}$$

where

$$\mathcal{T}_C = \sum_{j,\sigma} c^\dagger_{A_j\sigma} c_{C\sigma}, \qquad \mathcal{T}_\ell = \sum_{j,\sigma} c^\dagger_{A_{j+1}\sigma} c_{A_j\sigma}.$$

Here j is understood modulo 3, $U_A < 0$, and $U_C > 0$. The t_C terms generate the central anomalous-density test, while t_ℓ is the outer loop hopping needed for a winding state to represent a current-carrying branch rather than only a central cancellation texture. For the uniform texture the island phase vector is $(1, 1, 1)$. For the two winding textures it is

$$(1, \omega, \omega^2), \qquad (1, \omega^2, \omega), \tag{25}$$

with $\omega = e^{2\pi {\rm i}/3}$. The central phase sum obeys

$$1 + \omega + \omega^2 = 0. \tag{26}$$

Thus the winding branches node the active central repulsive site exactly, while the uniform branch drives a central anomalous-density antinode.

The C3 result is best viewed as a mechanism, not as the final physical device. Fixed-number exact-diagonalization diagnostics remain conservative, and full onsite-Hubbard HFB with Hartree and magnetic density relaxation drives the compact molecule to superconducting solutions with strongly suppressed anomalous amplitude in the sampled windows. The state is not assumed to be a true normal metal; rather, it is amplitude-starved after density relaxation. The Hartree field shifts the local levels in response to charge redistribution, so the few attractive orbitals in a compact molecule can be detuned away from the pairing-supporting regime while the repulsive centre remains costly. In that sense the relaxed Hartree field is not a small correction: in the finite microscopic molecules it is the mechanism that removes the condensate support needed to test the phase selector as a superconducting state. The compact rescue suggested by this diagnosis is not to freeze the density, but to add an externally imposed Hartree-compensation field or gate while still solving the HFG density equations; in notation, one replaces the normal onsite term by $\xi_i + \Sigma_i^{H,\rm ext} + U_i n_{i\bar\sigma}$ and asks whether a self-consistent superconducting branch survives near the intended effective level. This targeted test has been run for C3 molecules and clusters and for split/screw C4 compact variants. It confirms Hartree detuning as the failure mode but does not restore a robust compact superconducting winding state: strict roots either collapse to negligible anomalous

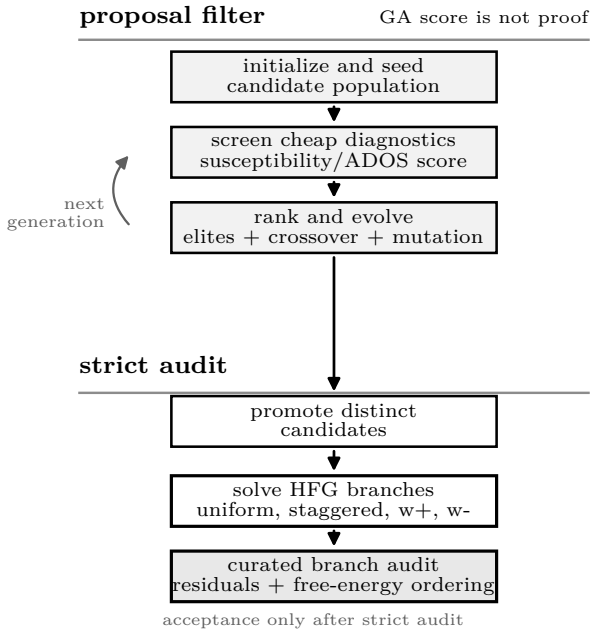

FIG. 4. Two-stage workflow used to propose island/channel geometries. The GA stage screens genomes with cheap susceptibility/ADOS diagnostics and promotes top distinct candidates rather than proving a phase. Promoted points are solved from uniform, staggered, and winding branch seeds; final acceptance is the later residual-controlled four-branch free-energy audit, not the GA score.

amplitude, below 10^{-9} in the over-compensated molecule tests, or remain accepted only with $|\Delta_A| \sim 10^{-5}$–10^{-4} in the hybrid cluster/channel refinements. Clusterizing each attractive site does not repair this by itself. C3 cluster scans through six attractive sites per island remain Hartree-detuned and amplitude-starved, with the largest mean attractive-island gap only 1.7×10^{-5}, and the complementary C4 cluster scans again separate constrained phase selection from unrestricted amplitude support.

A signed C3 crystal-bath control shows that the obstruction is not the interference rule itself. In this variant each active attractive site is coupled to an attractive dispersive reservoir orbital, while the central site keeps the same signed onsite update as the other local channels. The central-only benchmark removes the edge repulsive channels and therefore asks whether the symmetric positive-U_C site alone can select winding. A linear-susceptibility search is used only to propose a candidate; the reported point is then rechecked by full self-consistent HFG branch competition for the uniform and two winding seeds. At that tuned point the uniform seed develops a central antinode, $|\Delta_C| \simeq 0.64$, whereas both winding seeds retain the central node, $|\Delta_C| \lesssim 5\times10^{-11}$, and lie below the uniform branch by $\Omega_{\rm wind} - \Omega_{\rm uniform} \simeq -0.831$. This is a positive small-model existence smoke for the central-node mechanism, but it is also deliberately local: since the selection depends on cancellation of a costly anomalous antinode, some parameter sensitivity is expected. In a one-parameter-at-a-time $\pm8\%$ recheck around the stored point, 17/18 rows satisfy the strict selected-winding gate; the remaining chemical-potential row keeps a negative winding margin but misses the residual criterion.

Tube, crystal-bath, and proximity-film calculations then test ways of adding support. Tube models promote each molecule site into a one-dimensional periodic channel and average the onsite-Hubbard HFB fields over k_z; they can recover finite amplitude and node/antinode contrast after tuning, but the sampled rows remain nonwinding-led, and the soft-channel continuation crosses only after the winding anomalous amplitude collapses to $\sim 10^{-6}$. Proximity-film models take the complementary supplied-amplitude limit by adding fixed-amplitude phase terms, a branch-labelled anomalous self-energy, or explicit film sites whose pairing field is relaxed while the compact molecule is tested as a proximity-coupled selector. The strictest promoted balanced-screw finite-film row keeps $|\Delta_{\rm film}| \simeq 0.19$, selects winding by $\simeq 4.1\times10^{-7}$, and satisfies a maximum residual below 5×10^{-7}, whereas the simple periodic k-space anomalous self-energy bath remains uniform-led over the sampled grid. The later signed crystal-bath simulations go beyond this simple self-energy bath by adding pair-susceptible reservoir orbitals and local signed onsite updates; those runs are positive microscopic reservoir prototypes, while the proximity-film rows remain supplied-amplitude bridges.

A. Three-island bridge

The three-island model is the bridge between the molecular C3 rule and the later island device. Replacing each attractive site by a small superconducting island preserves the phase-sum cancellation at the central normal region while adding internal orbitals that can support amplitude. It also makes explicit that a loop supercurrent requires an outer path around the islands; the central node alone selects a phase texture but does not by itself provide a current-carrying circuit. At the phase-only level the central normal region contributes schematically

$$F_N \simeq \lambda_N \left| e^{\mathrm{i}\phi_0} + e^{\mathrm{i}\phi_1} + e^{\mathrm{i}\phi_2} \right|^2, \qquad \lambda_N > 0. \tag{27}$$

The uniform state maximizes this term, while the two C3 winding states cancel it. The isolated three-site and C3-cluster data therefore serve as a controlled bridge: they validate the interference rule, show the need for an outer loop path, and expose the Hartree-driven amplitude problem that motivates larger islands, proximity support, or pair-susceptible crystal baths.

V. C4 GEOMETRY AND SPLIT-SCREW REPAIR

For four islands, the relevant phase textures are

$$\begin{aligned} &(1,1,1,1), \qquad (1,\mathrm{i},-1,-\mathrm{i}),\\ &(1,-\mathrm{i},-1,\mathrm{i}), \qquad (1,-1,1,-1). \end{aligned} \tag{28}$$

The first is uniform, the next two are the time-reversed winding partners, and the last is staggered. The compact C4 Hamiltonian is usefully written by separating three classes of real hoppings:

$$\begin{aligned} H_{\rm C4} = H_A &- t_0 \sum_{j,\sigma} \left(c^\dagger_{A_j\sigma} c_{C\sigma} + \mathrm{h.c.} \right) \\ &- t_{\rm nn} \sum_{j,\sigma} \left[c^\dagger_{A_{j+1}\sigma} c_{B_j\sigma} + c^\dagger_{B_j\sigma} c_{A_j\sigma} + \mathrm{h.c.} \right] \\ &- t_{\rm split} \sum_{\sigma} \left(T_{02,\sigma} + T_{13,\sigma} + \mathrm{h.c.} \right) \\ &+ \sum_{r\in\{C,B_j,N_{02},N_{13}\}} U_r n_{r\uparrow} n_{r\downarrow}, \end{aligned}$$

where

$$H_A = \sum_{j,\sigma} \epsilon_A n_{A_j\sigma} + \sum_j U_A n_{A_j\uparrow} n_{A_j\downarrow}, \qquad U_A < 0,$$

$$\begin{aligned} T_{02,\sigma} &= c^\dagger_{A_0\sigma} c_{N_{02}\sigma} + c^\dagger_{N_{02}\sigma} c_{A_2\sigma}, \\ T_{13,\sigma} &= c^\dagger_{A_1\sigma} c_{N_{13}\sigma} + c^\dagger_{N_{13}\sigma} c_{A_3\sigma}, \end{aligned}$$

and the normal-region interactions U_r are positive or non-attractive. The central term proportional to t_0 is

the shared node test; the nearest-neighbour B_j paths are the staggered-favouring competitor; and the split/screw terms through N_{02} and N_{13} are the winding-favouring repair. A single central site is not a unique winding selector, because both winding and staggered textures have zero central phase sum. Moreover, a square molecule usually contains nearest-neighbour in-between normal paths; staggered order cancels those paths exactly. This is the central C4 difficulty.

The successful C4 design rule is to introduce separated diagonal or outer normal paths. In a compact split-centre molecule, this means two distinct normal loci: one coupled to the A_0, A_2 diagonal and one coupled to the A_1, A_3 diagonal. The split/screw construction effectively doubles the central normal node into separated loci. Schematic drawings should therefore treat the structure as screw-separated or effectively lifted out of the plane, not as a single planar crossing site. In the island language, the analogous design is a pair of outside normal paths. They penalize same-phase diagonal pairs and give the winding branch a node or suppression pattern on the relevant channel that the staggered branch does not share. The required normal sites and channels reduce the visual regularity of a planar square; the figure geometry is schematic and should not be read as a perfectly regular planar C4 molecule. Constrained compact scans confirm that screw-separated channels, unlike shared outside channels, select winding across broad sampled regions. This remains a phase-selection rule, not yet unrestricted microscopic superconducting ground-state evidence.

VI. MICROSCOPIC BOUNDARY

The isolated compact microscopic models are useful because they remove easy loopholes. They show that winding textures, winding nodes, and degenerate time-reversed partners are not hard to construct. They also show why compact cells are poor final devices. Full density relaxation, finite stiffness, and the uniform or staggered competitors usually erase the winding advantage.

The strongest bulk screw-cell calculation remains a near miss. After releasing the hard winding projection, the best winding branch remains a clean winding texture, with winding weight close to unity, but lies about 5.0×10^{-7} above the uniform branch. A sign-frustrated self-consistency ranking reaches a similar uniform-led margin of about 6.76×10^{-7}. This is evidence for a real metastable winding basin, not an artifact of branch labelling. It is still not a positive bulk ground-state result.

The common failure mode is stiffness and amplitude. Compact models make the loop short and rigid, while a few attractive orbitals do not reliably sustain a robust condensate after Hartree relaxation. This motivates the amplitude-reservoir formulations: signed crystal baths in the small microscopic setting and Josephson islands in the finite-device setting. The tube calculations show that adding a band can restore amplitude without yet producing a winding ground state in the sampled microscopic rows. The latest soft-channel tube continuation reinforces this distinction: reducing stiffness can invert the branch energy only after the winding anomalous amplitude is lost. The proximity-film calculations show one supplied-amplitude limit directly: a soft finite film can supply the condensate background that the relaxed Hartree field removes in isolated molecules, while a rigid or overly simple periodic self-energy bath and the baseline C4 geometry can still favour nonwinding cancellation. The later signed crystal-bath and Josephson-island models provide the stronger lesson: amplitude support must be self-consistent enough to survive Hartree feedback while still preserving the node/antinode selector. The calculation then asks whether the normal-channel geometry selects the phase texture.

VII. JOSEPHSON-ISLAND MODEL

The finite island model uses four superconducting islands connected to normal channels. Let S_a denote the set of sites in island a, $N_{\rm in}$ the inner normal channels, and $N_{\rm out}$ the long outer normal channels. The island-device Hamiltonian is

$$\begin{aligned} H_{\rm isl} = & \sum_{i,\sigma} (\epsilon_i - \mu_i) n_{i\sigma} - \sum_{(ij)\in E_{\rm isl},\sigma} t_{ij} \left(c^\dagger_{i\sigma} c_{j\sigma} + \text{h.c.} \right) \\ & - \sum_{(ij)\in E_{\rm in},\sigma} t_{ij} \left(c^\dagger_{i\sigma} c_{j\sigma} + \text{h.c.} \right) \\ & - \sum_{(ij)\in E_{\rm out},\sigma} t_{ij} \left(c^\dagger_{i\sigma} c_{j\sigma} + \text{h.c.} \right) \\ & + \sum_{i\in S} (-U) n_{i\uparrow} n_{i\downarrow} \\ & + \sum_{i\in N_{\rm in}} V n_{i\uparrow} n_{i\downarrow} + \sum_{i\in N_{\rm out}} W n_{i\uparrow} n_{i\downarrow}. \end{aligned}$$

Here $S = \cup_a S_a$. The edge sets $E_{\rm isl}$, $E_{\rm in}$, and $E_{\rm out}$ encode, respectively, hopping inside/proximal to the superconducting islands, inner contacts and channels, and the long outer channels used to lower winding stiffness. All t_{ij} are real; the four branch sectors are selected by initial self-consistency seeds rather than by Peierls phases. We compare four phase sectors: uniform, staggered, winding $+$, and winding $-$. All sectors are iterated to the same self-consistency standard, and the branch free energies are compared after convergence. The design target is a long or soft normal channel that supports a nonwinding antinode and a winding node. The long or soft channel reduces winding stiffness while keeping enough normal-channel anomalous density in the nonwinding branches to create an energy saving. The island result is accepted only if the uniform, staggered, winding $+$, and winding $-$ branches all satisfy the same residual threshold, the two winding partners are degenerate within numerical tolerance, and the common winding free energy lies below the best nonwinding branch.

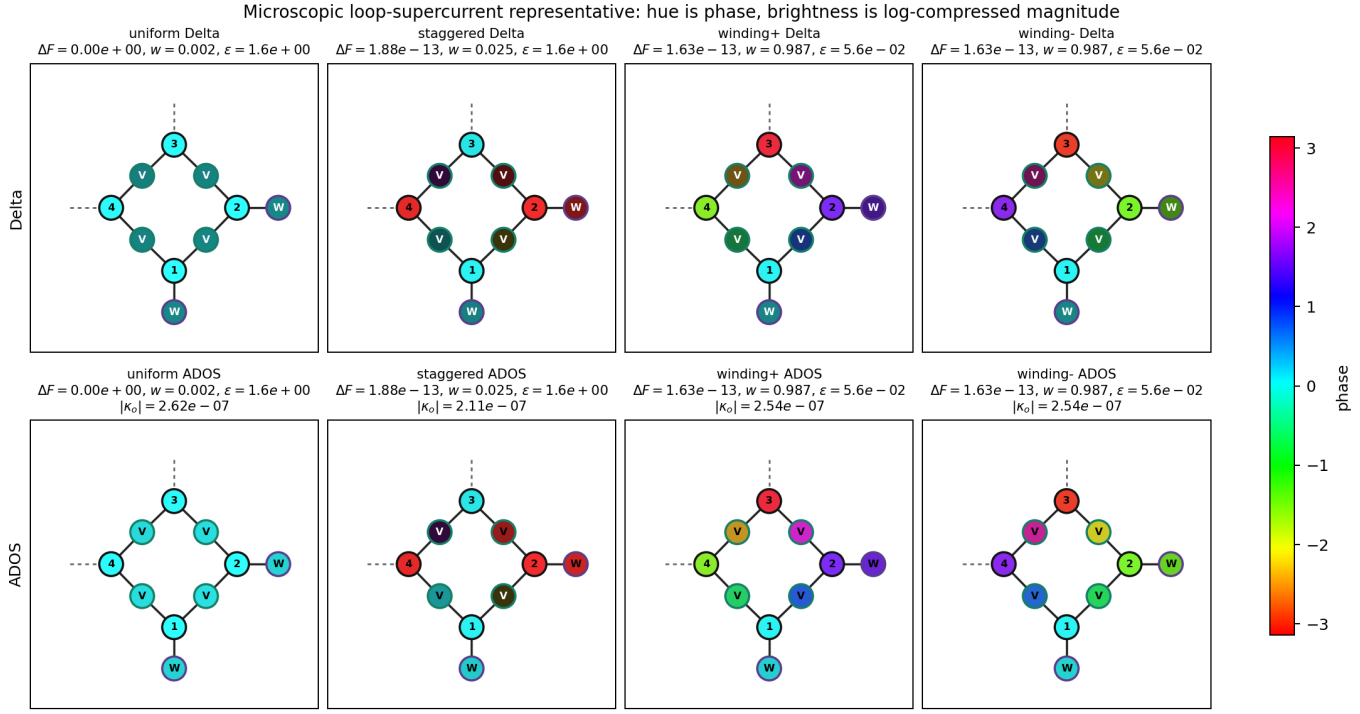

FIG. 5. Compact C4 microscopic anomalous-density examples. Rows show the self-consistent pairing field Δ and anomalous density (ADOS) for uniform, staggered, winding +, and winding − branches in a constrained four-site loop representative. Hue is phase and brightness is log-compressed magnitude. Panel annotations use $\Delta F = F_{\mathrm{branch}} - F_{\mathrm{min}}$, R for the final maximum self-consistency residual, $\overline{|\Delta|}$ for the mean pairing-field magnitude on the plotted superconducting sites, and $\overline{\mathrm{ADOS}}$ for the corresponding mean anomalous-density magnitude. The microscopic labels U, V, W, C denote the onsite attractive, inner-normal, outer-normal, and central-normal interactions used in that diagnostic run, and the μ's are the corresponding region chemical potentials. The outside normal channels contain one repulsive spacer each: W_{13} connects the 1–3 pair and W_{24} connects the 2–4 pair through periodic continuation. Dashed outside legs mark the continuation and are not additional normal sites. The example illustrates the microscopic texture logic used in the design search: winding branches can retain clean time-reversed phase structure and visible node/antinode rearrangement, even when the compact calculation remains a constrained or near-degenerate diagnostic rather than the final positive island ground-state result.

For the promoted long-soft outer-channel geometry `longer-outer2-soft-lower-mu`, the strict parameter point is

$$U = 2.0, \quad V/U = 0.2, \quad W/V = 1.0, \tag{29}$$

with

$$\mu_{\mathrm{island}} = 0, \quad \mu_{\mathrm{inner}} = -1.0, \quad \mu_{\mathrm{outer}} = -1.6, \tag{30}$$

and geometry parameters

$$\begin{gathered} L = 9, \quad h = 5, \quad h_{\mathrm{inner}} = 3, \\ \mathrm{separation} = 6, \quad \mathrm{outer\_length\_extra} = 2. \end{gathered} \tag{31}$$

The channel hoppings are

$$\begin{gathered} t_{\mathrm{outer\ channel}} = 0.5, \quad t_{\mathrm{inner\ contact}} = 0.5, \\ t_{\mathrm{outer\ contact}} = 1.0. \end{gathered} \tag{32}$$

Here F_{wind} denotes the common free energy of the two time-reversed winding branches within numerical tolerance, and $F_{\mathrm{nonwind}} = \min(F_{\mathrm{uniform}}, F_{\mathrm{staggered}})$. At this point the strict branch comparison gives

$$F_{\mathrm{wind}} - F_{\mathrm{nonwind}} \simeq -2.386 \times 10^{-3}, \tag{33}$$

with maximum residual 4.996×10^{-5} against a threshold of 5×10^{-5}. A second strict point at $\mu_{\mathrm{outer}} = -1.55$ remains winding-led by approximately -3.019×10^{-3}. Nearby W/V side points are winding-led at moderate convergence but not yet strict, and $\mu_{\mathrm{outer}} = -1.65$ returns to uniform. The residual is close to the stated acceptance threshold, so the convergence criterion and neighbouring-point status are quoted explicitly rather than treated as a robustness map. Thus the current result is a finite-device HFG existence result and a narrow tuned family, not yet a broad phase pocket.

VIII. CURRENT AND MAGNETIC-SCALE DIAGNOSTICS

Once a static branch has been selected by free energy, its loop-current character can be diagnosed from

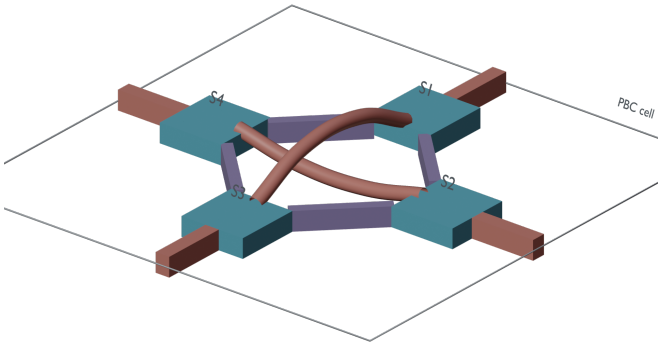

FIG. 6. Three-dimensional setup rendering of the promoted long-soft Josephson-island geometry. The blue pads mark the four extended superconducting islands, the red channels mark repulsive inner and outer normal channels, and the purple bars mark the diagonal winding channels. The two inner normal channels are drawn as a screw-inspired over/underpass: one channel is lifted across the other rather than forming a single planar crossing node. This is a schematic device realization of the split/screw selector idea, in which separated normal loci distinguish winding from the staggered competitor. The inner over/underpass is a geometric visualization of the selector logic rather than an additional proof ingredient; if retained as additional repulsive selector channels, such central channels would further lower the node-forming winding and staggered branches relative to the uniform branch. The render emphasizes the modeling distinction between compact molecular sites and a device with extended superconducting reservoirs plus normal selector channels. It is a geometric visualization only; the ground-state evidence remains the static four-branch HFG free-energy comparison, and the anomalous-density texture is shown separately in Fig. 8.

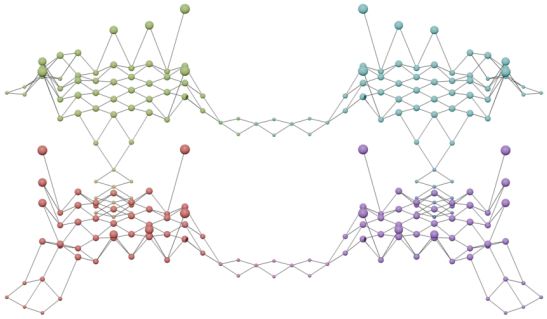

FIG. 7. Three-dimensional anomalous-density rendering for the promoted island geometry. The four coloured sheets show branch-resolved ADOS magnitude and phase on the extended islands and channels. This view is included to make the real-space winding texture legible in the device geometry; it is a diagnostic visualization, while the branch ordering is still determined by the static four-branch HFG free-energy comparison and the quantitative ADOS montage in Fig. 8.

the hopping-current operator. For a real hopping t_{ij} the bond current from i to j is

$$I_{ij} = \frac{2e}{\hbar}\,\mathrm{Im}\left[t_{ij}\sum_{\sigma}\langle c^{\dagger}_{i\sigma}c_{j\sigma}\rangle\right], \tag{34}$$

with $I_{ji} = -I_{ij}$. A scalar circulation diagnostic can be formed by summing the tangential component around a chosen loop contour $\mathcal{C}$,

$$I_{\mathrm{loop}} = \frac{1}{|\mathcal{C}|}\sum_{(ij)\in\mathcal{C}} s_{ij} I_{ij}, \tag{35}$$

where s_{ij} fixes the positive orientation. The time-reversed winding partners have opposite I_{loop} by construction and are degenerate in the absence of imposed flux.

For an order-of-magnitude magnetic diagnostic, the orbital moment associated with a planar loop current is

$$m_z \simeq I_{\mathrm{loop}} A_{\mathrm{eff}}, \tag{36}$$

where A_{eff} is the effective enclosed area of the current path. Equivalently, a bond-resolved estimate uses

$$\boldsymbol{m} = \frac{1}{2}\sum_{(ij)} \boldsymbol{r}_{ij}\times I_{ij}\boldsymbol{\ell}_{ij}, \tag{37}$$

with $\boldsymbol{r}_{ij}$ the bond midpoint and $\boldsymbol{\ell}_{ij}$ the directed bond vector. For the promoted island point we evaluate Eq. (34) from the converged BdG one-body density matrix and then form the finite-cell version of this bond-resolved moment from the local current segments. These expressions define the conversion from dimensionless lattice currents to an order-of-magnitude magnetic moment once a lattice spacing, hopping scale, and effective loop area are specified. They are not ground-state evidence; the static branch free-energy comparison remains the evidence for selection.

The same diagnostic can be converted to material scales by inserting a microscopic length and electronic energy. For a scale estimate relevant to the LaNiX_2 compounds cited in the TRSB background, take $a_{\mathrm{eff}} = V_{\mathrm{cell}}^{1/3}$ from the spin-orbit QE cell volumes recorded in the verification bundle and set $I_0 = eE_0/\hbar$. Using $E_0 = 10\,\mathrm{meV}$ gives the estimates in Table II. The signs are opposite for the two time-reversed winding partners; the table reports absolute values. These numbers are conversions of the island-current diagnostic, not predictions that $LaNiC_2$ or $LaNiGa_2$ realize the island-device ground state.

IX. DYNAMICAL CONTROL OUTLOOK

Time-dependent SCMFT/HFG provides a natural diagnostic and control proposal for the selected winding pair. Starting from one converged winding minimum,

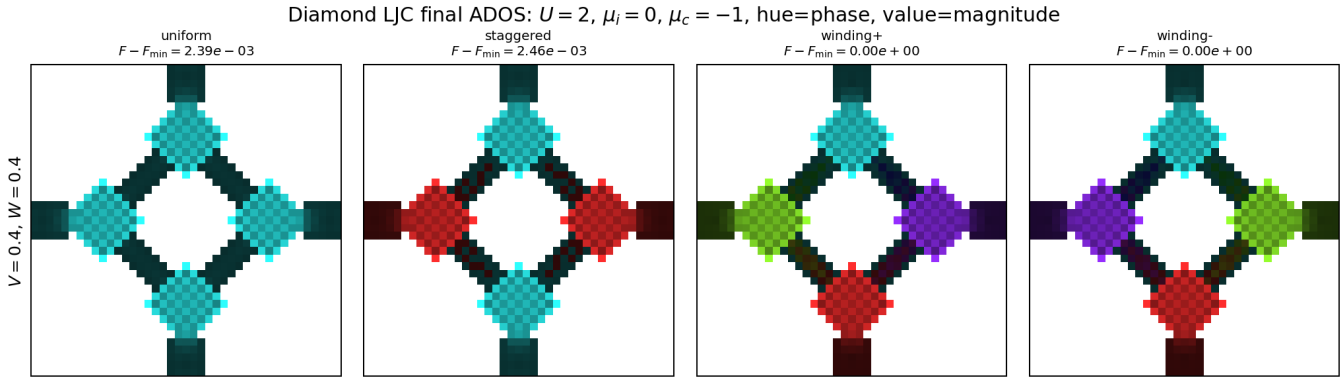

FIG. 8. Complex anomalous-density textures for the promoted island geometry. The four panels show the final self-consistent ADOS for uniform, staggered, winding +, and winding − branches. Hue records complex phase and value records magnitude. The header gives the island-device parameters, and the panel annotations use $\Delta F = F_{\text{branch}} - F_{\min}$ and R for the final maximum field residual. The "averaged" label indicates that the displayed scalar summaries are mean magnitudes over the plotted island/channel sites. The winding branches are time-reversed partners of the same strict minimum.

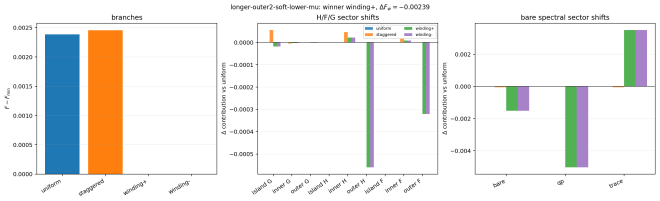

FIG. 9. Free-energy decomposition for the promoted long-soft island point. The branch comparison is the selection evidence: the winding branch is below the best nonwinding branch after the same strict self-consistency criterion is applied to all branches.

TABLE II. Material-scale conversion of the promoted-island current diagnostic using $a_{\text{eff}} = V_{\text{cell}}^{1/3}$ from local LaNiX_2 QE cells and $E_0 = 10\,\text{meV}$. The moment and angular momentum scale linearly with E_0.

material	a_{eff} (nm)	$\lvert m_z\rvert/\mu_B$	$\lvert L_z\rvert/\hbar$
$LaNiC_2$	0.482	6.05×10^{-2}	6.05×10^{-2}
$LaNiGa_2$	0.683	1.21×10^{-1}	1.21×10^{-1}

a short local phase, chemical-potential, or weak vector-potential pulse could couple the two time-reversed sectors and monitor whether the loop-current diagnostic in Eq. (34) reverses sign. Such a protocol would test whether the device behaves as a controllable winding qubit in the low-energy subspace spanned by the two TRSB partners. This is a dynamical response proposal, not a substitute for the static ground-state claim. The latter is the strict HFG free-energy ordering in Eq. (33).

X. DISCUSSION

The result should be stated at the correct level. We have not established a broad robust phase diagram. Within the finite-device HFG calculation, we have established that a time-reversal-symmetric island Hamiltonian can select a pair of degenerate time-reversed winding minima without external flux. The microscopic studies explain why isolated compact attractive-orbital models fail: they either lose amplitude through Hartree detuning or pay too much winding stiffness. The newer bath simulations show one way around that failure in small models: pair-susceptible reservoir orbitals compensate the Hartree amplitude loss while retaining the split-centre or central-node selector. The island model is the corresponding finite-device realization, where larger superconducting reservoirs supply amplitude and soft channels reduce stiffness.

This distinction also clarifies the role of dynamics. Time-dependent HFG and current animations are useful presentation diagnostics because they visualize the selected current-carrying branch. They do not determine the ground state. The ground-state claim rests on the static strict four-branch HFG free-energy comparison.

The same distinction suggests a sharper route for future microscopic searches. A superconducting amplitude-support mechanism is not, by itself, a mechanism for spontaneous TRSB. The missing ingredient may instead be a selector for the time-reversal-odd loop-current variable

$$\chi_{\square} = \sum_{\langle ij\rangle \in \square} \text{Im}\left[t_{ij}\langle c_i^{\dagger} c_j\rangle\right], \tag{38}$$

or for the corresponding coarse-grained orbital moment. A time-reversal-symmetric microscopic Hamiltonian can only select spontaneous circulation through an even functional of this variable, such as an effective $-K_{\chi}\chi_{\square}^2$, leav-

ing the two signs of $\chi_\square$ degenerate. A linear field conjugate to $\chi_\square$ is useful for susceptibility tests, but it is not a spontaneous-TRSB mechanism. This motivates several controlled next tests: unrestricted complex-bond Fock feedback, nearest-neighbour interactions decoupled in current-current or bond-current channels, nearly degenerate real bond-order modes whose complex combination is chiral, plaquette-flux susceptibility pre-screens with the field removed after diagnosis, and paired clockwise/counter-clockwise seed tests that require degenerate final free energies. These tests would decide whether the island result can be traced back to a local or short-range microscopic selector rather than to a phenomenological loop-current stiffness term. As a first reduced benchmark in this direction, a projected current-channel Fock feedback on the compact C4 outside-junction molecule can produce a narrow intermediate-coupling window in which the time-reversed winding pair is selected with finite island amplitude. The stricter fully complex density-density Fock benchmark, which keeps both real bond renormalisation and imaginary current order in the same loop, is much more fragile: only a small weak-coupling winding-selected point survives before the amplitude collapses or a nonwinding branch returns. This comparison must also be interpreted with gauge care: a phase in an individual Fock bond field can be redistributed into the anomalous phase texture by a local rephasing, so the diagnostic quantity is the closed-loop combination

$$\Phi_{\mathrm{rel}} = \sum_{\langle ij\rangle\in\square} \arg[-h_{ij}^{\mathrm{eff}}] + \frac{1}{2}\sum_{\langle ij\rangle\in\square} \arg(\Delta_j\Delta_i^*) \pmod{2\pi}, \tag{39}$$

rather than the phase of one bond field alone. A companion gauge-loop re-ranking benchmark, $\Omega_{\mathrm{eff}} = \Omega_0 - K_\Phi(1-\cos\Phi_{\mathrm{rel}})^2$, selects the same time-reversed winding pair at the representative outside-junction C4 point once $K_\Phi \simeq 0.026$; this identifies the loop-phase stiffness that a microscopic mechanism would need to generate. The corresponding self-consistent current-current feedback check, with a loop field updated as $\Phi = 2K_\chi\chi_\square$, does produce paired equal-and-opposite flux fixed points but does not select the compact C4 winding branch over the nonwinding competitor in the tested range. Repeating the same feedback on the split-centre C4 graph can make the winding pair lowest in the reduced branch ranking, but the selected winding solution is amplitude-starved and therefore fails the finite-amplitude criterion used for a superconducting loop-current state. An amplitude-support scan then shows the complementary lesson: when the effective island attraction is increased in the same split-centre reduced model, converged finite-amplitude winding cells appear at low to moderate loop-feedback strength. This does not add an explicit one-handed TRSB field, but it is still a reduced diagnostic rather than an unrestricted material calculation. A more microscopic-adjacent version replaces this stronger-island-attraction knob by one attractive auxiliary bath orbital hybridized to each island. In that split-centre bath benchmark, the bath sector develops a large branch-symmetric gap, and sufficiently strong island-bath hybridization transfers enough amplitude back to the islands to obtain converged finite-amplitude winding rows while preserving the degeneracy of the two time-reversed partners. Releasing the branch projection at the representative bath-supported point gives the next check: the island and bath gaps are updated as unrestricted complex onsite fields, and the final winding is classified only after convergence. In that seed-release scan, the named winding seeds converge to the lowest finite-amplitude solutions, while uniform and staggered seeds converge to higher reduced mean-field energies. Random and asymmetric seeds are retained as small basin probes, not as an exhaustive basin-of-attraction map. Replacing each auxiliary bath level by a two-site attractive bath chain gives a first finite-spectrum version of the same mechanism. The named winding seeds remain lowest over the sampled t_D, t_{DD} grid, and the strict converged finite-winding criterion is satisfied once the island-bath hybridization is moderate or strong; the weakest hybridization column is finite-amplitude and winding-led but remains marginal under the quick convergence gate. A four-level bath-ring variant gives a stronger finite-reservoir check: over the sampled moderate/strong hybridization grid, all cells remain converged, finite-amplitude, and winding-led. Adding reference-subtracted onsite Hartree feedback gives a mixed but useful result: screened Hartree scales preserve the finite-amplitude winding solution, whereas the unscreened onsite Hartree update leaves winding energy-ranked but collapses the condensate amplitude below threshold. Adding a projected current-channel Fock field on top of the screened bath-band calculation gives the next compatibility check. At the representative $s_H = 0.2$ point, the self-consistent update of the island-bond field $Q_{ij} = \langle c_i^\dagger c_j\rangle$, projected as $Q_{ij} \mapsto i\,\mathrm{Im}\,Q_{ij}$, preserves the finite-amplitude winding minimum through the converged window $s_F \le 2$. The largest sampled point remains winding-ranked but misses the strict residual gate, so this is not a broad phase diagram. It is nevertheless a useful microscopic-adjacent benchmark: amplitude support, screened density feedback, and a loop-current selector can coexist in one HFG loop, but the result still relies on projecting out the real bond-renormalisation channel that competes in the fully complex Fock test. A stricter follow-up keeps the fully complex bond field in the same screened finite bath-band model. Unlike the compact outside-junction molecule, this bath-supported split-centre geometry remains converged, finite-amplitude, and winding-led at the sampled $s_F = 0, 1, 2$ points even when both $\mathrm{Re}\,Q_{ij}$ and $\mathrm{Im}\,Q_{ij}$ are retained. The fully complex update gives a larger normal bond-field scale and a slightly weaker winding margin than the projected-current update, so real bond renormalisation is still visible, but it does not destroy the representative bath-supported winding solution. The mechanism target is therefore sharper: one needs an amplitude-supporting bath, band, or interaction chan-

nel together with the split-centre phase selector, rather than a scalar loop-current feedback acting on a fragile compact molecule alone. In a crystal, such a bath should be understood as additional reservoir orbitals, tubes, or layers that generate normal and anomalous self-energies on the active loop sector after hybridisation, not merely as a larger copy of the compact loop. If active orbitals a hybridise with reservoir bands b through $T(\mathbf{k})$, integrating out the reservoir gives schematically

$$\begin{aligned} \Sigma_a(\mathbf{k}, i\omega_n) &= T(\mathbf{k})[i\omega_n - h_b(\mathbf{k})]^{-1} T^\dagger(\mathbf{k}), \\ \Delta_a^{\mathrm{ind}}(\mathbf{k}, i\omega_n) &\sim T(\mathbf{k}) F_b(\mathbf{k}, i\omega_n) T^T(-\mathbf{k}), \end{aligned} \tag{40}$$

where F_b is a reservoir anomalous Green function or pair susceptibility. The previous tube and Bloch-lattice tests show that adding dispersion alone is insufficient; the next microscopic target is an orbital- or layer-selective reservoir that supplies amplitude and screened Hartree environment while leaving the split-centre loop selector in the active subspace. A first code-level prototype of this type, with one dispersive reservoir orbital per island, selects the finite-amplitude winding pair in a screened fully complex HFG run; the result survives $N_{k_z} = 2, 3, 4, 6$ and a small hybridization/bandwidth map. Initial controls show a detuning boundary and, more importantly, a normal-only bath with $U_D = 0$ fails to produce a finite active winding state, whereas attractive bath interactions restore bath amplitude, active amplitude, and negative winding margin. With the pair-susceptible bath fixed, turning on explicit split-centre and edge repulsive pairing-penalty sites leaves the solution finite-amplitude and makes the winding margin more negative relative to the zero-penalty control, so the penalty sites act as an additional selector contribution rather than a replacement for the amplitude reservoir. An explicit outside-channel control then separates the geometry further: opposite-pair normal penalty sites connecting 1–3 and 2–4 also drive the best seed into the winding sector, while adding nearest-neighbour edge penalties weakens the margin in the sampled point. A stricter signed-onsite HFG variant, in which the same local update $\Delta_i = -U_i F_i$ is applied also on the positive-U normal sites, weakens the margins but preserves the accepted finite-winding split-centre and split-plus-opposite rows. This is a sanity check for the crystal-bath mechanism, not yet a thermodynamic or materials-realistic phase diagram. Repeating the signed-onsite reservoir construction in the C3 geometry gives an independent small-model smoke test of the same mechanism: a threefold active triangle with one pair-susceptible dispersive reservoir orbital per active site selects the degenerate winding pair over the uniform seed with finite active and bath amplitudes. This C3 result is deliberately recorded as a representative existence check; broader k_z-mesh, detuning, and interaction scans are still needed before treating it as a C3 phase diagram.

XI. CONCLUSION

The calculations give a deliberately narrow but explicit route to spontaneous loop supercurrents. A time-reversal-symmetric Hamiltonian can select two degenerate time-reversed winding branches when the device geometry makes those branches suppress anomalous density on repulsive normal regions that are active in non-winding states. The resulting Gor'kov saving is a real-space interference effect, not an imposed Peierls phase or a chiral pairing assumption.

The negative microscopic results are part of the mechanism. Compact C3 molecules give the clean node rule, while C4 molecules expose the staggered competitor. Clusters, Hartree-biased compact scans, lattices, and tubes then show why the node rule alone is not enough: isolated compact attractive orbitals are Hartree-detuned or amplitude-starved, and periodic normal backgrounds or tube bands do not by themselves promote a finite-amplitude winding branch to the lowest unrestricted branch in the sampled rows. The follow-up simulations sharpen this boundary: a softer tube can invert the branch ordering only after the winding amplitude collapses, Hartree-referenced hybrid clusters remain amplitude-starved at accepted residuals, whereas tuned reservoir-band controls can keep finite amplitude and a winding advantage. Thus the current positive microscopic message is no longer only "go to islands": pair-susceptible baths can also compensate the Hartree loss in controlled C3/C4 HFG prototypes, although broad parameter maps and material-derived realizations remain open.

The promoted long-soft Josephson-island device supplies the missing ingredient by separating superconducting amplitude support from the soft repulsive channels that perform the phase selection. Its strict four-branch HFG free-energy comparison is the ground-state evidence in this finite model. Current, magnetic-scale, three-dimensional, and dynamical diagnostics identify the selected branch as a loop-supercurrent state, but they do not replace the static free-energy ordering. The result is therefore a controlled finite-device existence result and a narrow tuned family, not yet a broad phase diagram.

Appendix A: Genetic-search implementation details

The implemented susceptibility-screening score has the schematic form

$$\begin{aligned} S_{\mathrm{GA}} = B_{\mathrm{wind}} - d_{wu} - \frac{1}{2} d_{ws} + R_{\mathrm{out}} + R_{\mathrm{surv}} + R_C \\ - P_{\mathrm{stag}} - P_{\mathrm{in}} - P_{\mathrm{raw}} - P_{\mathrm{sing}}. \end{aligned} \tag{A1}$$

Here d_{wu} and d_{ws} are the susceptibility-ranking gaps between the best winding node and the best uniform or staggered competitor, and B_{wind} is nonzero only when the best inverse-susceptibility label is winding-like. The reward block contains outer-node saving, winding-unique

outer saving, useful outer and central antinode terms, island-survival terms, frustration advantage, outer-over-inner selectivity, and a near-degeneracy bonus. The penalty block subtracts staggered outer saving, staggered outer competition, inner saving, staggered inner saving, raw unselective outer and inner responses, poor outer-over-inner selectivity, inner antinodes, and singular outliers.

The focused susceptibility profile samples

$$\mu_i \in [-3.6, -2.0], \quad \mu_c \in [-2.0, 1.6], \quad W/V \in [0.6, 4.0],$$

with nominal spacings $0.1, 0.1, 0.2$, respectively; it also samples $V = 0.08, 0.12, \ldots, 0.36$, $U \in \{2.0, 2.5\}$, separations $3, \ldots, 11$, outer-strip widths $3, 5, 7$, inner-radius extras $1, 2, 3$, and inner-corner radii $2, 3, 4$. The wide profile extends these to $\mu_i \in [-3.8, -1.8]$, $\mu_c \in [-2.4, 1.8]$, $W/V \in [0.4, 5.0]$, $V = 0.04, \ldots, 0.44$, $U \in \{1.8, 2.0, 2.25, 2.5\}$, separations $3, \ldots, 15$, outer-strip widths $3, 5, 7, 9$, inner-radius extras $0, \ldots, 4$, and corner radii $0, 2, 3, 4, 5$. Chemical potentials, V, and W/V are treated as continuous controls during crossover and mutation; the remaining geometry controls are discrete.

Each row records the genome, generation number, scalar score, best inverse-susceptibility label, winding-versus-uniform and winding-versus-staggered node-ranking gaps, and the node/antinode metrics used by the score. Before evaluating a proposed genome, the code builds a quantized duplicate key from lattice size, separation, interactions, chemical potentials, strip geometry, inner-sheet geometry, and C4 boundary flags. One generation evaluates uncomputed genomes, ranks the accumulated rows, keeps elites, creates crossover/mutation children, and fills the remaining population slots by random injection. The focused susceptibility stage uses a population of 96, 24 elites, 16 random injections, mutation probability 0.55, mutation width of two grid steps, eight generations, seed 20260514, and 24 worker processes.

The active HFG-promotion stage maps a susceptibility genome into the nonlinear outer-sheet-strip HFG case with matched outer gaps and C4-symmetric, plaquette-centred bounds. Its default search uses 72 genomes, 18 elites, 12 random injections, six HFG promotions per generation, mutation probability 0.55, a two-step global mutation width, and 18 local refinements around confirmed HFG elites with local mutation width 0.35. The promoted HFG runs use tolerance 2×10^{-4}, damping $\gamma = 0.08$, and 24 self-consistency iterations in the active-search stage; later curated mechanism checks tighten these settings for manuscript points. Confirmed active-search rows are ranked by a separate diagnostic score that rewards winding winners, outer-channel Gor'kov saving, winding-unique outer-locus suppression, and island ADOS survival, while penalizing inner-channel saving, staggered outer-locus saving, and bare stiffness cost. The final paper point was not accepted on either proxy score. It was accepted only after the curated four-branch HFG comparison gave the winding pair the lowest free energy at the stated residual threshold.

ACKNOWLEDGMENTS

The calculations were performed with a private general-purpose codebase developed by the author. The accompanying verification bundle records the public model specifications, parameter tables, benchmark outputs, intermediate checks, and numerical figure data for independent reimplementation.

[1] B. D. Josephson, Physics Letters **1**, 251 (1962).
[2] P. W. Anderson and J. M. Rowell, Physical Review Letters **10**, 230 (1963).
[3] V. Ambegaokar and A. Baratoff, Physical Review Letters **10**, 486 (1963).
[4] K. K. Likharev, Reviews of Modern Physics **51**, 101 (1979).
[5] A. A. Golubov, M. Y. Kupriyanov, and E. Il'ichev, Reviews of Modern Physics **76**, 411 (2004).
[6] A. J. Leggett, Reviews of Modern Physics **47**, 331 (1975).
[7] M. Sigrist and K. Ueda, Reviews of Modern Physics **63**, 239 (1991).
[8] C. C. Tsuei and J. R. Kirtley, Reviews of Modern Physics **72**, 969 (2000).
[9] A. D. Hillier, J. Quintanilla, and R. Cywinski, Physical Review Letters **102**, 117007 (2009).
[10] A. D. Hillier, J. Quintanilla, B. Mazidian, J. F. Annett, and R. Cywinski, Physical Review Letters **109**, 097001 (2012).
[11] S. K. Ghosh, G. Csire, P. Whittlesea, J. F. Annett, M. Gradhand, B. Ujfalussy, and J. Quintanilla, Physical Review B **101**, 100506 (2020).
[12] L. N. Bulaevskii, V. V. Kuzii, and A. A. Sobyanin, JETP Letters **25**, 290 (1977).
[13] L. P. Gor'kov, Soviet Physics JETP **7**, 505 (1958).